7

Interpretation of Results

This chapter presents first attempt of interpretation of the measured data. The obtained asymmetries, presented in section 6.8, will be confronted by the theoretical predictions of the Bochum/Krakow group. The comparison with the calculations will be done separately for all three reaction channels $^3\vec{\mathrm{He}}(\vec{e}, e'd)p$, $^3\vec{\mathrm{He}}(\vec{e}, e'p)d$ and $^3\vec{\mathrm{He}}(\vec{e}, e'p)pn$. A special attention will be dedicated to the first two channels, which are currently under better control. The extraction and interpretation of the asymmetries for the latter channel is presently confined by an inaccurate separation of the three-body breakup events from the two-body breakup events. The comparison with the previous double-polarization asymmetry measurement from Mainz will also be performed. In the end, the conclusions will be drawn, together with a summery of open problems and challenges for the future work.

7.1 The two-body breakup channel $^3\vec{\mathrm{He}}(\vec{e}, e'p)d$

The experimental asymmetries shown in Figs. 6.31 to 6.33, where proton is detected by the BigBite, are hybrids combined of the $^3\vec{\mathrm{He}}(\vec{e}, e'p)d$ and $^3\vec{\mathrm{He}}(\vec{e}, e'p)pn$ asymmetries. The relative contribution of each reaction channel is governed by the ratio of cross-sections for the two processes. To isolate the asymmetry corresponding to the reaction $^3\vec{\mathrm{He}}(\vec{e}, e'p)d$, the two-body breakup events (2BBU) must be separated from the three-body breakup events (3BBU).

This is accomplished by inspecting the missing energy histogram, where 2BBU events generate a peak around $E_{Miss} = 5.5\,\mathrm{MeV}$, while 3BBU events gather around $E_{Miss} = 7.7\,\mathrm{MeV}$. The obtained peaks are usually smeared by the radiative losses and limited resolutions of the spectrometers. Present analysis has shown (see Fig. 7.1), that for the E05-102 data, these effects are so large, that two-body breakup peak can no longer be distinguished from the the three-body peak. This represents an important obstacle in the interpretation of our results and requires a use of Monte-Carlo simulation for a proper comparison of the theory to the measured data

Unfortunately a detailed simulation for E05-102 experiment is not yet available. Instead, an approximate empirical approach was considered, for this first extraction of the 2BBU asymmetries. In this procedure measured $(e, e'p)$ asymmetries were plotted as a function of missing energy. Obtained results are shown in Fig. 7.2. Here only events with low missing momentum $p_{Miss} \leq 90\,\mathrm{MeV/c}$ were acknowledged. In this

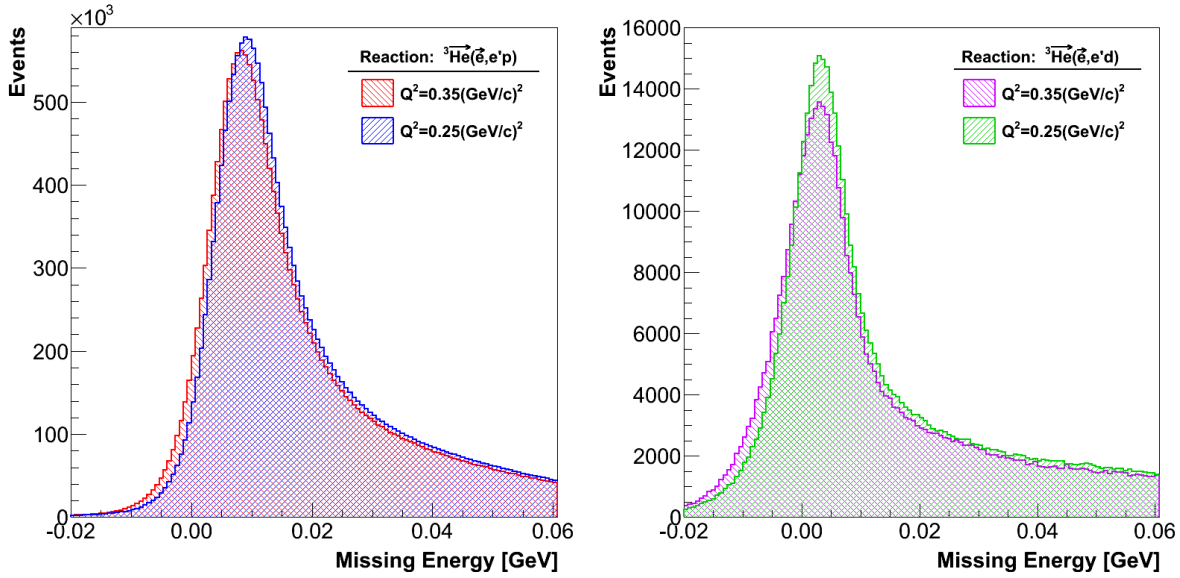

Figure 7.1 — The reconstructed missing energy (E_{Miss}) distributions for reactions $^3\vec{He}(\vec{e},e'p)$ (left) and and $^3\vec{He}(\vec{e},e'd)p$ (right). Histograms show results for both kinematical settings: $Q^2 \approx 0.35,\ 0.25\,(GeV/c)^2$. Due to the radiative effects and poor spectrometer resolutions, the 2BBU and 3BBU peaks in the proton channel can not be distinguished.

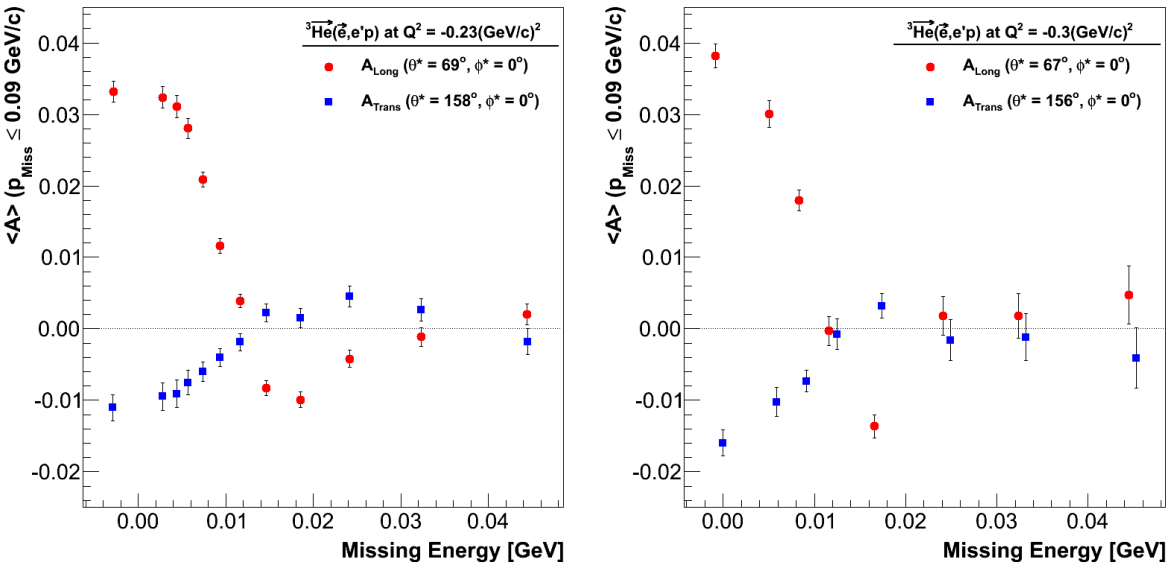

Figure 7.2 — Asymmetries as a function of missing energy E_{Miss}. Left and right plot show longitudinal and transverse asymmetries for kinematical settings $Q^2 = -0.23\,(GeV/c)^2$ and $Q^2 = -0.3\,(GeV/c)^2$ respectively. Each data point represents an average asymmetry for missing momenta between $p_{Miss} = 0 - 90\,MeV/c$.

limit is the S-state dominates the ^{3}He-wave function, and encourages a large asymmetry in the case of the 2BBU and almost a zero asymmetry for the 3BBU (see Sec. 2.5 for more detail). The measured asymmetry agrees well with this hypothesis. A large positive asymmetry was discovered in a region of small E_{Miss}, where 2BBU governs. When moving to higher E_{Miss} , the asymmetry eventually decreases towards zero. In

that region the 3BBU is expected to dominate. A negative asymmetry in the middle region ($E_{Miss} \approx 15\,MeV$) is a result of an interactions between nucleons. The Mainz experiment [30] has described this with the FSI, that are expected to generate a strong effect in the 3BBU channel at low E_{Miss}. This also explains a rapid drop of the asymmetry at $E_{Miss} \approx 6MeV$, where the 3BBU process starts to contribute. At higher E_{Miss} the strength of the FSI weakens and the asymmetry closes to zero.

An almost flat asymmetry at very low missing energies indicates a dominance of the 2BBU reaction in that region. Relaying on this assumption, the 2BBU asymmetries were extracted from the measurements, by selecting only events with $E_{Miss} \leq 1.6\,MeV$. Both longitudinal and transverse asymmetries were obtained. Results for both kinematical settings are gathered in Fig. 7.3.

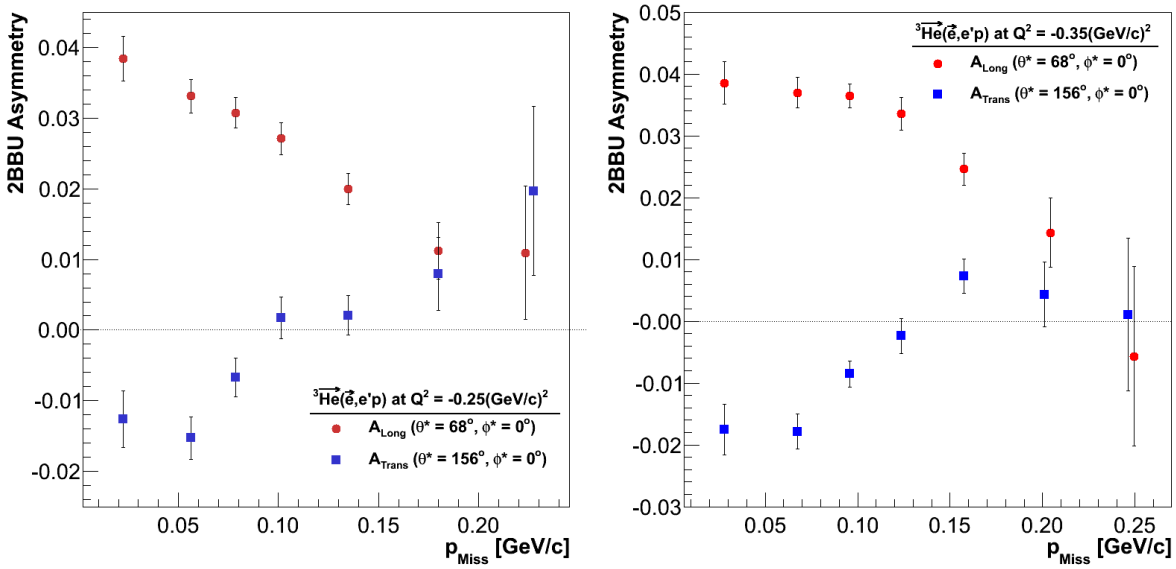

Figure 7.3 — The longitudinal and transverse $^3\vec{He}(\vec{e}, e'p)d$ asymmetries at $Q^2 = -0.23\,(GeV/c)^2$ (left) and $Q^2 = -0.3\,(GeV/c)^2$ (right). The asymmetries were determined by selecting only measurements with $E_{Miss} \leq 1.6\,MeV$.

The determined approximate 2BBU asymmetries are now ready to be challenged by the theoretical predictions. The calculations were performed by the Bochum/Krakow group [117]. They were able to perform calculation of asymmetries for eleven different kinematics points, that are gathered in Table 7.1 and shown in Fig. 7.4. They are comfortable performing calculations only for $Q^2 \lesssim 0.3\,(GeV/c)^2$. Hence, points were selected to cover the whole kinematical acceptance for the experimental setting, when HRS-L is positioned at scattering angle of $\theta_{HRS-L} = 12.5°$. The bin with highest statistics was divided even further into three smaller bins. Kinematical points at $Q^2 > 0.3\,(GeV/c)^2$, that are accessible when HRS-L positioned at $\theta_{HRS-L} = 14.5°$ were not considered. The theory will therefore be tested mostly with the $Q^2 = -0.25\,(GeV/c)^2$ data. However, since the kinematical acceptances of the two experimental setups overlap in region around $Q^2 = -0.3\,(GeV/c)^2$, some checks could also be performed with the data, that were taken with $\theta_{HRS-L} = 14.5°$.

Beside the information on the electron kinematics and target spin orientation (θ^*, ϕ^*), the theoretical calculations as an input require also the momentum of a detected proton $\tilde{p}$ and the polar angle θ_p for each selected bin in missing momentum p_{Miss}. Here,

Table 7.1 — The list of eleven kinematic points considered in the theoretical calculations. The points are selected to cover the kinematical acceptance for the setting when HRS-L is positioned at $\theta_{HRS-L} = 12.5°$. The section with highest statistics was further divided into three smaller bins. The Bochum/Krakow group is able to predict asymmetries for each of the points separately. The size of the momentum transfer vector q for each combination of E, E′ and θ_e was obtained via the Mainz kinematic calculator [116].

Kinematic Points for Theory

i	E [MeV]	E′ [MeV]	θ_e [deg]	q [MeV/c]	ω [MeV]
1	2425.5	2.235	11.35	498.2	190.5
2	2425.5	2.268	11.35	488.0	157.5
3	2425.5	2.285	11.35	485.0	140.5
4	2425.5	2.302	11.35	485.0	123.5
5	2425.5	2.335	11.35	480.0	90.5
6	2425.5	2.235	12.45	538.7	190.5
7	2425.5	2.285	12.45	526.9	140.5
8	2425.5	2.335	12.45	519.8	90.5
9	2425.5	2.235	13.55	579.8	190.5
10	2425.5	2.285	13.55	570.7	140.5
11	2425.5	2.335	13.55	567.7	90.5

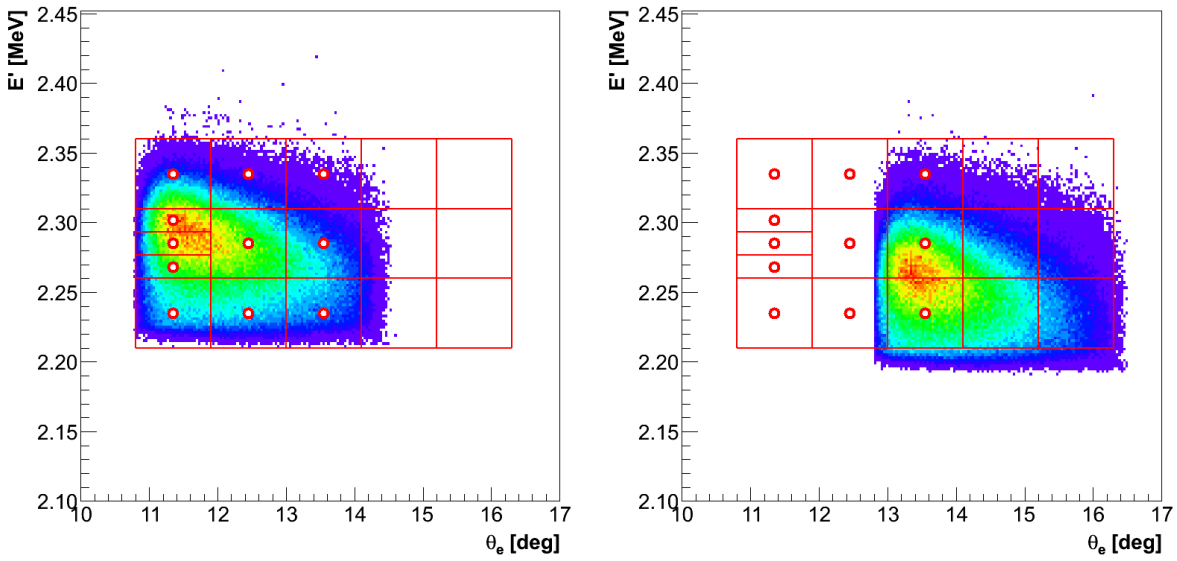

Figure 7.4 — The electron kinematics accessible when HRS-L was positioned at $\theta_{HRS-L} = 12.5°$ (left) and at 14.5° (right). The whole kinematical coverage was divided into 17 bins, demonstrated with red squares. Theoretical calculations were performed for the centers of first 11 bins (denoted with circles).

θ_p represents an angle between the momentum transfer vector $\vec{q}$ and proton momentum $\vec{p}$ (see Fig. 2.2). Considering the conservation of energy and momentum in the non-relativistic limit, theoreticians use θ_p to calculate the momentum of the detected

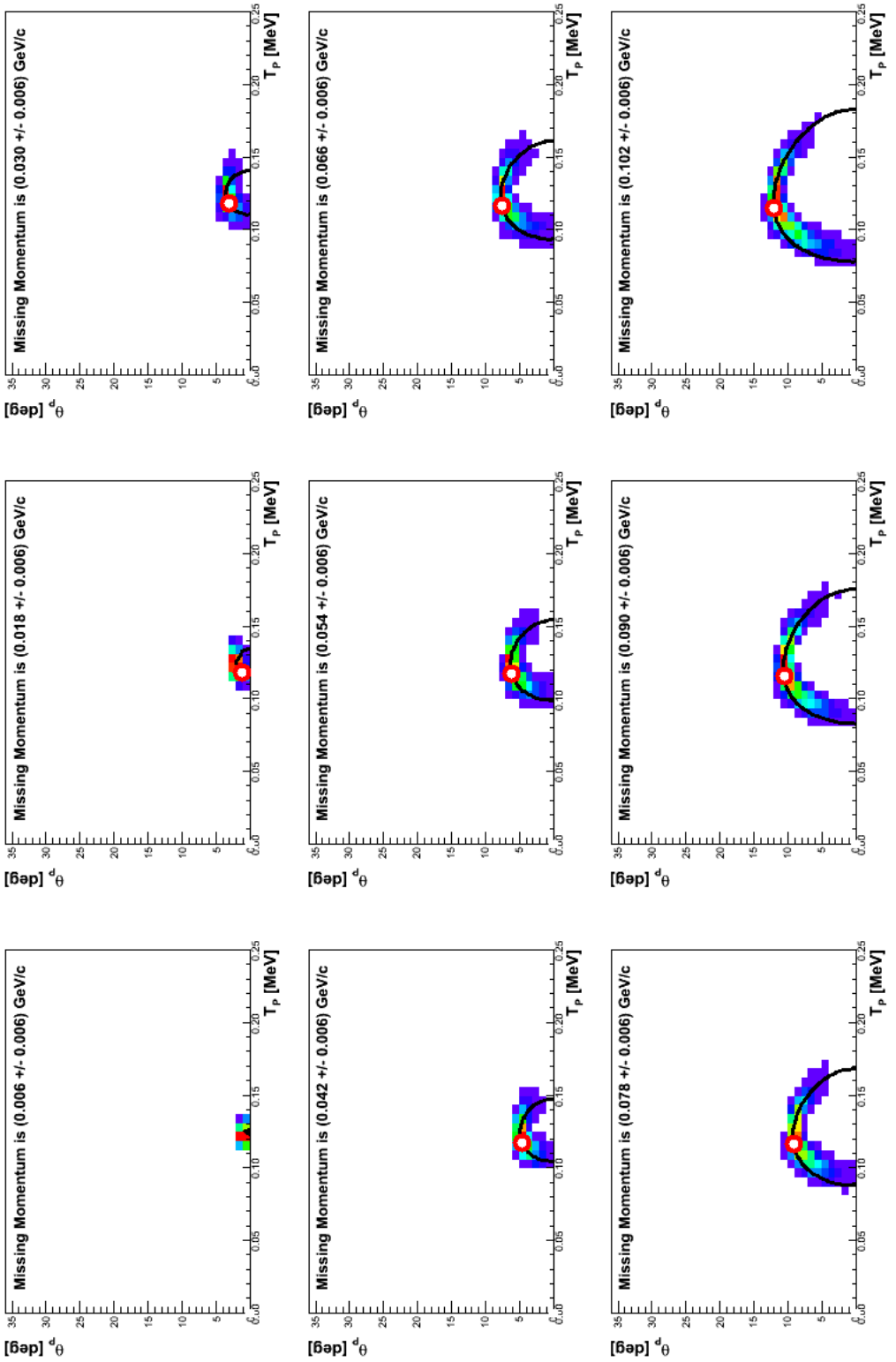

Figure 7.5 — Two-dimensional histograms are showing relation between proton angle θ_p and its kinetic energy $T_p \approx p^2/2M_p$, for selected bins in p_{Miss}. In these plots only data from the 4^{th} kinematics bin were considered (see Fig. 7.4). The lengths of the obtained bands are controlled by the remaining spread in ω and $\vec{q}$. Black lines show solutions of Eq.(7.2) for a given p_{Miss} and $|\vec{q}| = 485.0\,\text{MeV/c}$. Circles show $(\theta_p, \tilde{p})$ pairs considered in the theoretical calculations. For the 4^{th} kinematic point, events with very low missing momenta are not accessible. Hence, theoretical point is missing in the histogram for $p_{Miss} = 6\,\text{MeV}$.

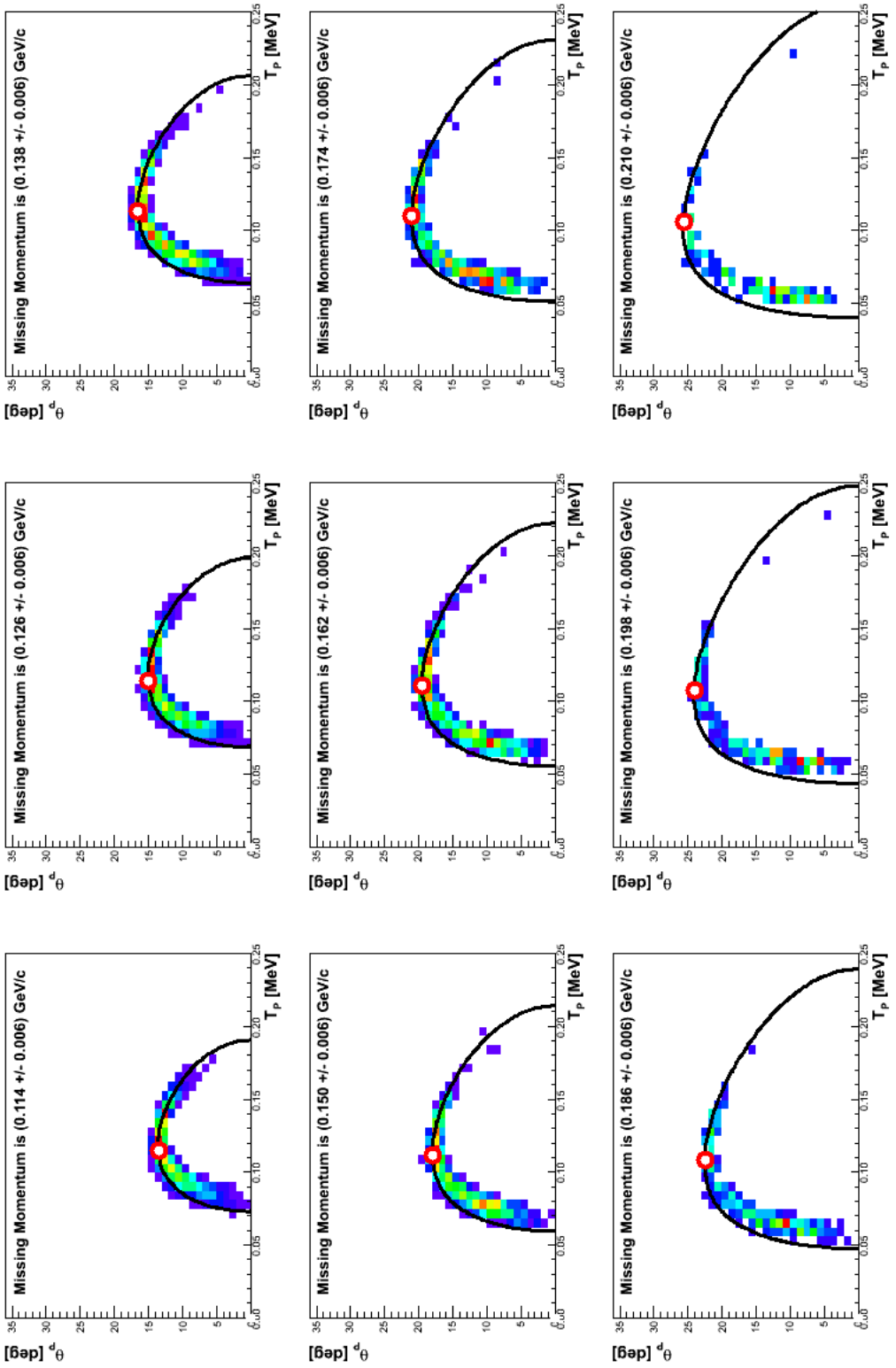

Figure 7.6 — Two-dimensional histograms are showing relation between proton angle θ_p and its kinetic energy $T_p \approx p^2/2M_p$, for selected bins in p_{Miss}. In these plots only data from the 4^{th} kinematics bin were considered (see Fig. 7.4). The lengths of the obtained bands are controlled by the remaining spread in ω and $\vec{q}$. Black lines show solutions of Eq.(7.2) for a given p_{Miss} and $|\vec{q}| = 485.0\,\mathrm{MeV/c}$. Circles show $(\theta_p, \tilde{p})$ pairs considered in the theoretical calculations.

proton p, independently of the input parameter $\tilde{p}$:

$$\text{Conservation of Energy :} \quad \omega + M_{^3\text{He}} = M_p + M_{\text{Miss}} + \frac{\vec{p}^2}{2M_p} + \frac{\vec{p}_{\text{Miss}^2}}{2M_{\text{Miss}}}\,, \quad (7.1)$$

$$\text{Conservation of Momentum :} \quad \vec{p}^{\,2}_{\text{Miss}} = \vec{q}^{\,2} + \vec{p}^{\,2} - 2|\vec{p}|\,|\vec{q}|\cos\theta_p\,. \quad (7.2)$$

Here, p_{Miss} and M_{Miss} are the momentum and the mass of the undetected deuteron. Inserting Eq.(7.2) into Eq.(7.1), a quadratic equation for the proton momentum p is obtained:

$$p = \frac{(2M_p q\cos\theta_{pq}) \pm \sqrt{(2M_p q\cos\theta_{pq})^2 - 4(M_p + M_{\text{Miss}})(M_p q^2 - 2M_p M_{\text{Miss}} - H)}}{2(M_p + M_{\text{Miss}})}\,,$$

where $H = \omega + M_{^3\text{He}} - M_p - M_{\text{Miss}}$. Equation has two solutions, and algorithm chooses the one, closest to the input momentum $\tilde{p}$. This way parameter $\tilde{p}$ serves only for selecting the physical solution of the equation. This procedure is utilized as an protection mechanism before any non-physical combinations of $\tilde{p}$ and the polar angle θ_p used in the calculations. In spite of this safety precaution, only proper combinations of the two parameters should introduced to the code. Non-matching combinations of $\tilde{p}$ and θ_p would result in asymmetry calculations for different p_{Miss}, than desired.

The correct pairs $(\theta_p, \tilde{p})$ for each p_{Miss} bin were obtained from the corresponding two-dimensional histograms. The analysis was done separately for every kinematic bin. The obtained distributions for the 4^{th} bin are demonstrated in Figs. 7.5 and 7.6. In spite of the tight kinematical cuts, the accepted events still have some freedom in ω and $\vec{q}$. Consequently, data for each p_{Miss} bin are not gathered in a single point, but form a band. The shape of the band is dictated by the Eq. 7.2, while its length is governed by the spread in $omega$ and $\vec{q}$. The pairs $(\theta_p, \tilde{p})$ considered in the asymmetry calculations are labeled with circles. They also represent points, where all the data would be gathered, if the chosen kinematical bin would be reduced to an infinitesimally small section of data around the chosen kinematical point. Unfortunately such narrow cuts can not be performed on data, because then all the statistics would be lost.

Once the input data was available, the theoreticians could perform calculations for all eleven kinematic points. For each target orientation and each bin in missing momentum, they generated asymmetries as functions of the angle ϕ_p. The calculated longitudinal and transverse asymmetries for 4^{th} kinematic point are shown in Figs. 7.7 and 7.8, respectively.

The experimental results are not separated in terms of bins in ϕ_p. The theoretical calculations must therefore be averaged over the angle ϕ_p in order to compare them to the measured asymmetries. A proper averaging over the ϕ_q is crucial for correct interpretation of the calculations, since theoretical asymmetries at $p_{\text{Miss}} \geq 100\,\text{MeV/c}$ have a strong angular dependence. This procedure is not trivial, since the ϕ_p distribution depends strongly on both, selected kinematical point and p_{Miss}. Fig. 7.9 shows the ϕ_p distributions for various p_{Miss}, obtained for 4^{th} kinematic point. In the region of low missing momenta, angles around $\phi_p \approx 180^\circ$ dominate. When moving towards the higher missing momenta, the events with $phi_p \approx 90^\circ, 270^\circ$ become superior.

An appropriate averaging of the calculated asymmetries was achieved by generating the ϕ_p histograms for each p_{Miss} in all eleven kinematic bins. The obtained distributions were then considered as weights in the weighted average formula, that was

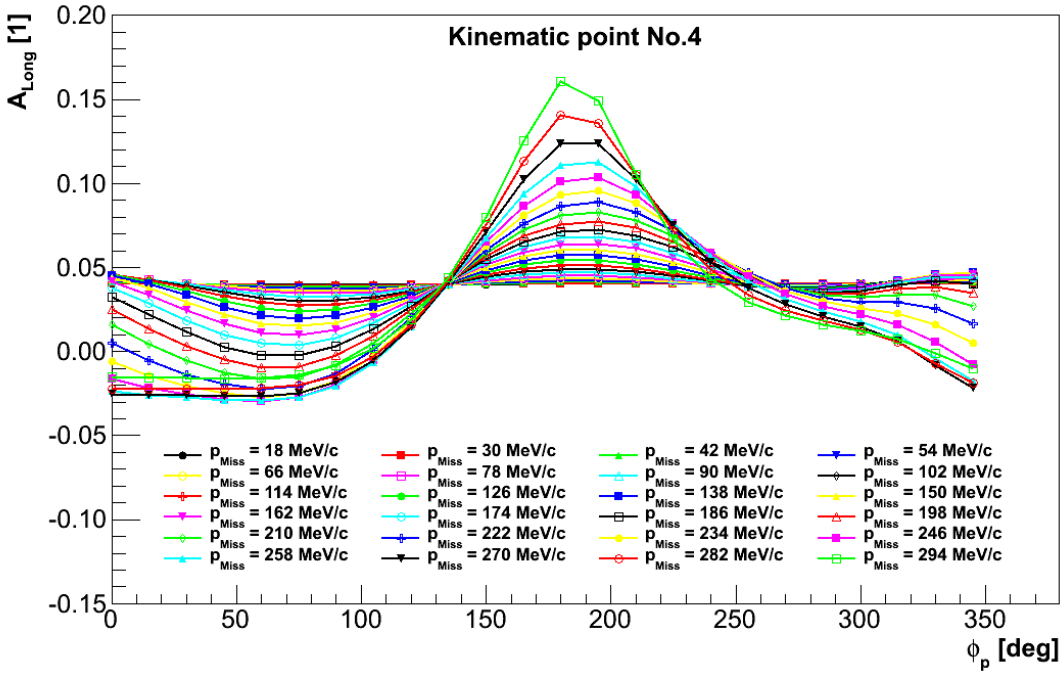

Figure 7.7 — The theoretical predictions for the longitudinal $^3\vec{\mathrm{He}}(\vec{e}, e'p)d$ asymmetry $A_{\mathrm{Long}} = A(\theta^* = 68°, \phi^* = 0°)$ as a function of angle ϕ_p, for various missing momenta up to $p_{\mathrm{Miss}} \leq 300\,\mathrm{MeV}$. Presented asymmetries were determined for the 4^{th} kinematic point. Calculations were provided by the Bochum/Krakow group [117].

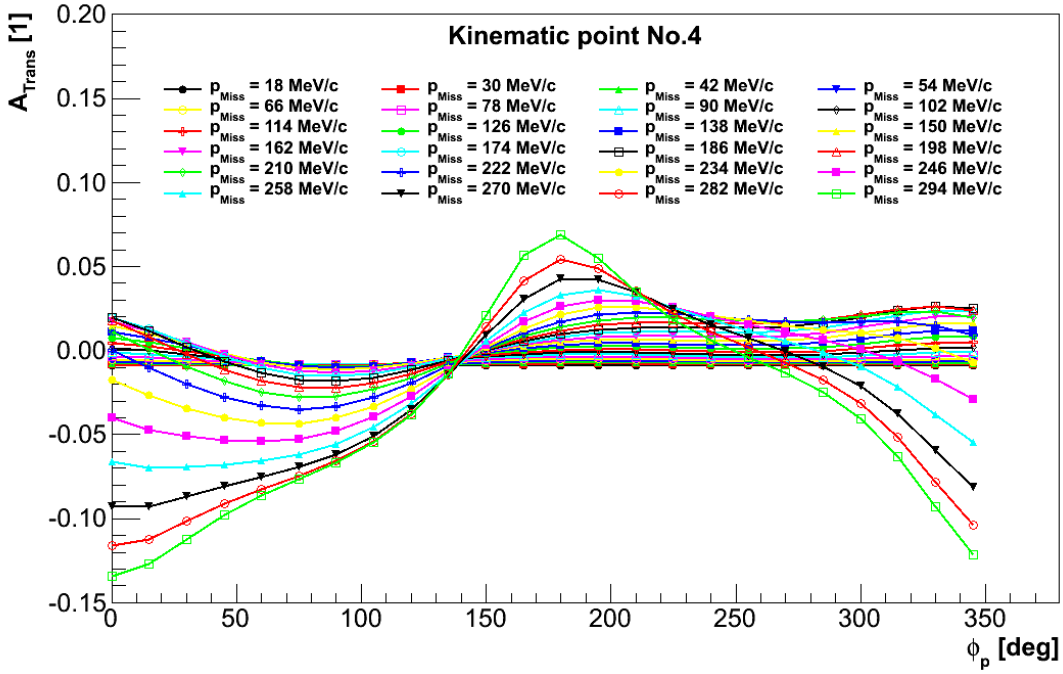

Figure 7.8 — The theoretical predictions for the transverse $^3\vec{\mathrm{He}}(\vec{e}, e'p)d$ asymmetry $A_{\mathrm{Trans}} = A(\theta^* = 156°, \phi^* = 0°)$ as a function of angle ϕ_p, for various missing momenta up to $p_{\mathrm{Miss}} \leq 300\,\mathrm{MeV}$. Presented asymmetries were determined for the 4^{th} kinematic point. Calculations were provided by the Bochum/Krakow group [117].

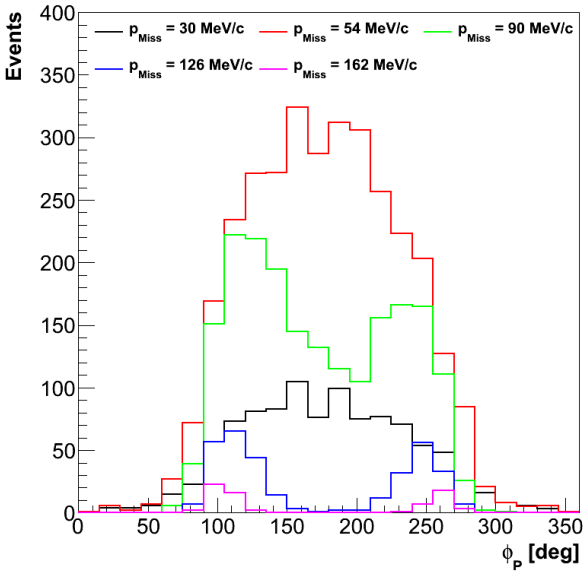

Figure 7.9 — The distributions of ϕ_p at different p_{Miss}, determined for the events gathered around the 4th kinematic point. At low missing momenta, the angles near $\phi_p = 180°$ dominate. At higher missing momenta, events with $\phi_p \approx 90°, 270°$ prevail.

utilized for the ϕ_p averaging of the asymmetries:

$$\overline{A}(p_{Miss}) = \frac{\sum_{\phi_p^i} A(p_{Miss}, \phi_p^i) N_{\phi_p^i}}{\sum_{\phi_p^i} N_{\phi_p^i}},$$

where ϕ_p^i goes over all bins in the $\phi_p(p_{Miss})$ distribution and $N_{\phi_p^i}$ represents the number of events in each of the bins. $A(p_{Miss}, \phi_p^i)$ represent calculated asymmetries shown in Figs. 7.7 and 7.8, while $\overline{A}(p_{Miss})$ is the resulting average asymmetry for a chosen p_{Miss}.

After the average asymmetries were calculated for all p_{Miss} available for a selected kinematic point, they could be compared to the measured asymmetries. Separate comparisons were done for each kinematic points. Such comparisons are only approximate since each of the eleven calculated asymmetries describes only one section of data, while the experimental asymmetries represent an average over whole acceptance. Hence, for a rigorous comparison, averaging over whole kinematical acceptance has to be performed, combining the theoretical asymmetries of all eleven kinematic points. This requires an understanding of the asymmetry behavior in regions between two calculated points. The interpolation of the calculated asymmetries to the whole kinematic acceptance has not been addressed yet and represents one of the challenges for the future work.

In spite of these open problems, comparison of the calculations, corresponding to individual kinematic points, to the data, already provide some important findings. Fig. 7.10 shows results for the most populated 4th kinematical point. This is also the only point, which brings information on the asymmetries at low missing momenta. All other kinematic points provide data only at higher missing momenta. With the exception of the points at lowest missing momenta, the calculated asymmetries do not agree with the measured data. They have consistent signs, and also have similar trends, but the absolute values are very different. For example, the experimental asymmetry A_{Long} seems to be decreasing much faster towards zero than the calculated one, which remains at values $\approx 4\,\%$. The inspection of the rest of the calculations has shown similar behavior of the predicted asymmetries also in all other kinematical bins. Some examples are shown in Figs. 7.10 and 7.11. This means, that experimental asymmetries at

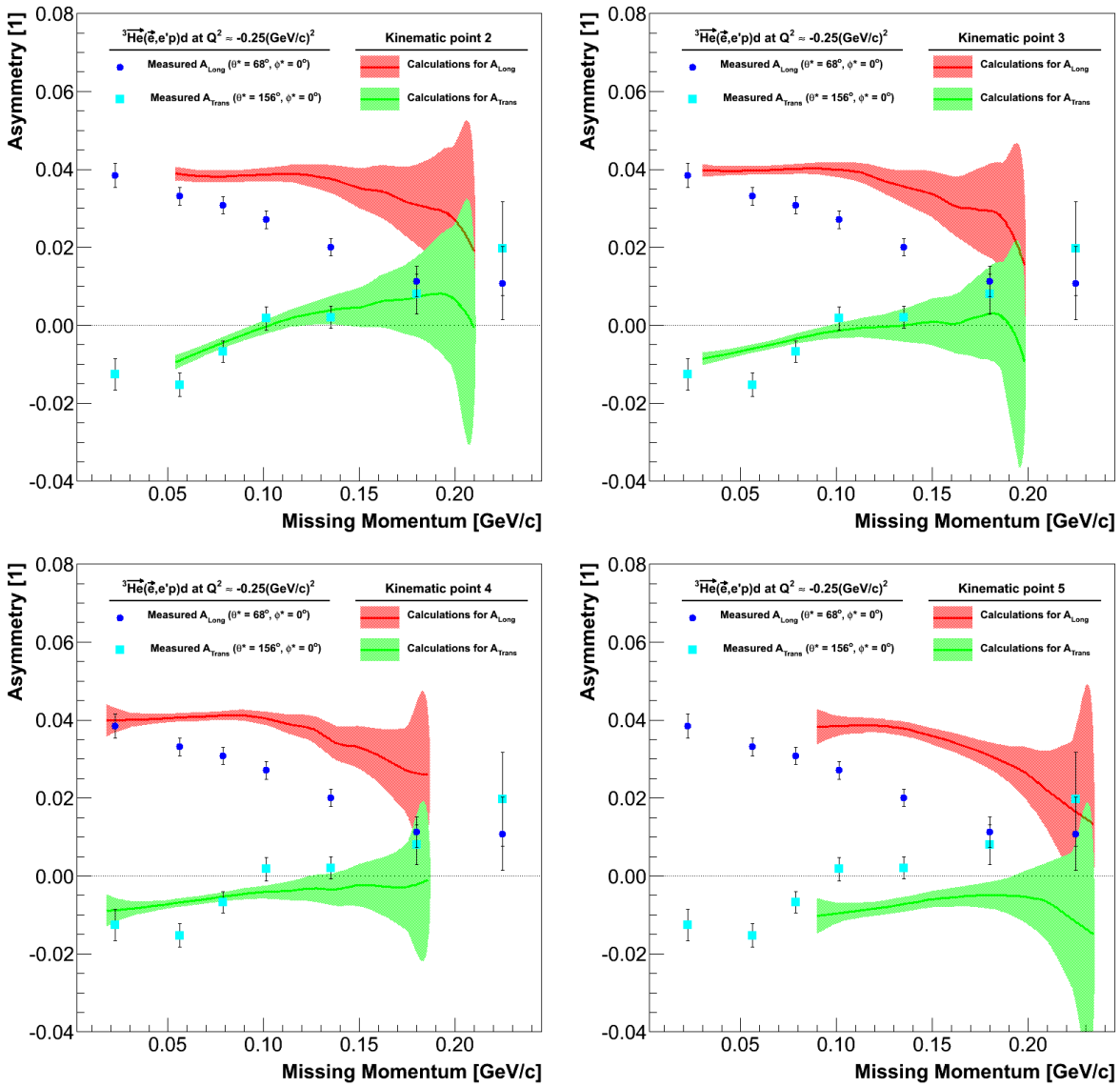

Figure 7.10 — Comparison of the calculated $^3\vec{He}(\vec{e},e'p)d$ asymmetries for the 2^{nd} 3^{rd}, 4^{th} and 5^{th} kinematic bin with the extracted experimental asymmetries at $Q^2 = -0.25\,(GeV/c)^2$. The theoretical asymmetries are shown with full lines. The surrounding bands demonstrate the uncertainties of the predicted asymmetries, and are governed by the statistics in the ϕ_p-histograms (see Fig. 7.9) used for the averaging of the calculated asymmetries.

high missing momenta could not be properly described by this theory, not even with the proper averaging of the calculations over the whole kinematic acceptance. Identical problems appear also with the comparison of the calculations for 9^{th}, 10^{th} and 11^{th} kinematic point to the $Q^2 = -0.35\,(GeV/c)^2$ measurements. These results are shown in Fig. 7.12. Finding the reason for this persisting discrepancy between the data and the theory therefore presents another dare, that needs to be resolved in the future.

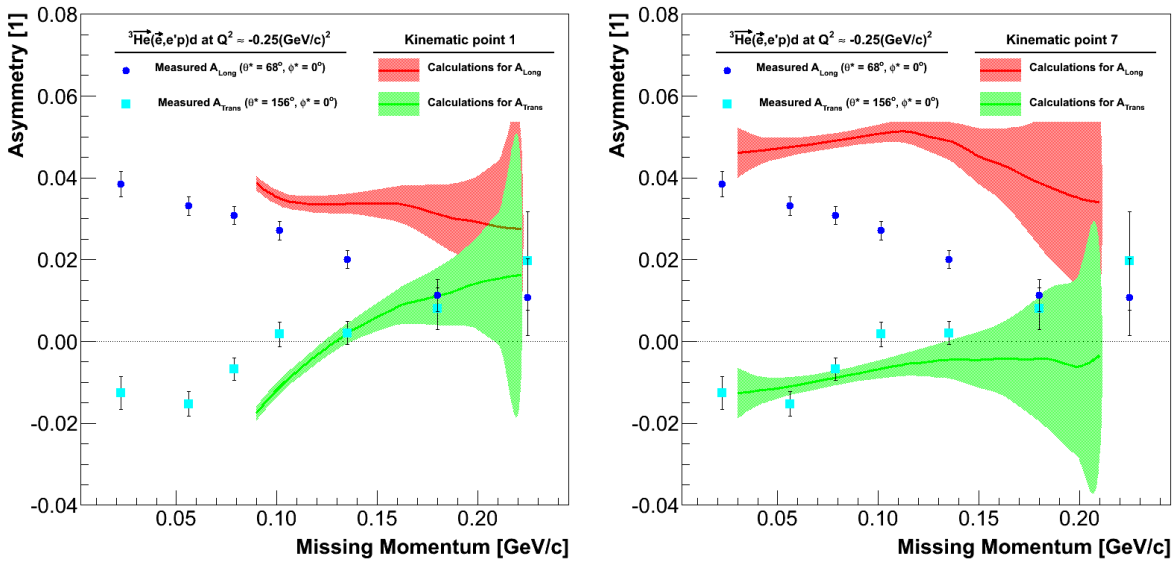

Figure 7.11 — Comparison of the calculated asymmetries for the 1st and 7th kinematic bin with the extracted experimental $^3\vec{He}(\vec{e},e'p)d$ asymmetries at $Q^2 = -0.25\,(GeV/c)^2$. The theoretical asymmetries are shown with full lines. The surrounding bands demonstrate the uncertainties of the predicted asymmetries for each bin in missing momentum, which are governed by the statistics of the ϕ_p-histograms (see Fig. 7.9) used for the averaging of the calculated asymmetries over the angle ϕ_q.

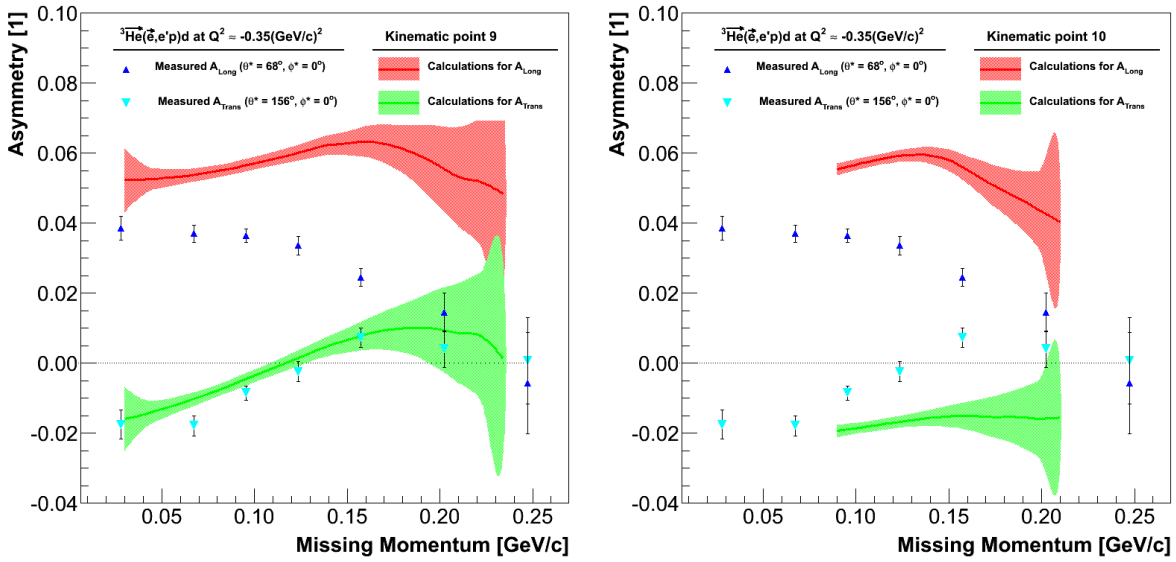

Figure 7.12 — Comparison of the calculated asymmetries for the 9th and 10th kinematic bin with the extracted experimental $^3\vec{He}(\vec{e},e'p)d$ asymmetries at $Q^2 = -0.35\,(GeV/c)^2$. The theoretical asymmetries are shown with full lines. The surrounding bands demonstrate the uncertainties of the predicted asymmetries for each bin in missing momentum, which are governed by the statistics of the ϕ_p-histograms (see Fig. 7.9) used for the averaging of the calculated asymmetries over the angle ϕ_q.

7.2 Relation to elastic scattering on $\vec{p}$

In a very simple picture can the ^{3}He ground-state be imagined as a bound state of a deuteron and a proton. In this case can the spin-part of the ^{3}He wave-function be expressed in terms of Clebsh-Gordan coeficients as:

$$\begin{aligned} |J = 1/2, m_J = 1/2\rangle_{^3\mathrm{He}} &= \sqrt{\frac{2}{3}} |J = 1, m_J = 1\rangle_d |J = 1/2, m_J = -1/2\rangle_p \\ &- \sqrt{\frac{1}{3}} |J = 1, m_J = 0\rangle_d |J = 1/2, m_J = 1/2\rangle_p \,, \end{aligned} \tag{7.3}$$

where J and m_J represent the spin of a particle and the size of its third component, respectively. The expression (7.3) can be used to estimate the polarization of the proton inside the nucleus. When the ^{3}He nucleus is polarized along the z-axis, the proton polarization P_p can be written as:

$$P_p = {}_{^3\mathrm{He}}\langle 1/2, 1/2|\ 2\,\hat{\sigma}_z^p\, P_{^3\mathrm{He}}\ |1/2, 1/2\rangle_{^3\mathrm{He}} = P_{^3\mathrm{He}} \left[\frac{2}{3}\left(-\frac{2}{2}\right) + \frac{1}{3}\left(\frac{2}{2}\right)\right] = -\frac{1}{3} P_{^3\mathrm{He}} \,,$$

where $P_{^3\mathrm{He}}$ is the effective polarization of the helium, and $\hat{\sigma}_z^p$ is the Pauli matrix, utilized to project proton spin to the z-axis. When ^{3}He is 100 % polarized, the proton polarization is $P_p \approx -33.3\,\%$. The negative sign of polarization means, that proton spin is predominantly oriented in the direction opposite to the nuclear spin.

This naive model of the ^{3}He can be further used to approximately describe the two-body electrodisintegration process $^3\vec{\mathrm{He}}(\vec{e}, e'p)d$ at low missing momenta. In this limit, the virtual photon interacts only with a proton, while leaving the deuteron as a spectator at rest (see Sec. 2.5). By neglecting any interaction between proton and deuteron, this process can be approximated with the elastic scattering of electrons on polarized proton target $\vec{p}(\vec{e}, e'p)$. This means, that the extracted $^3\vec{\mathrm{He}}(\vec{e}, e'p)d$ asymmetries at $p_{\mathrm{Miss}} \approx 0$, should agree with the elastic proton asymmetry $A_{\vec{e}\vec{p}}$, corrected for the effective proton polarization inside the ^{3}He:

$$A_{2\mathrm{BBU}}(p_{\mathrm{Miss}} = 0, \theta^*, \phi^*) \approx -\frac{1}{3} A^{\vec{e}\vec{p}}(\theta^*, \phi^*) \,. \tag{7.4}$$

To test this hypothesis, the asymmetry ratios $A_{2\mathrm{BBU}}/A^{\vec{e}\vec{p}}$ were calculated for four data points closest to the $p_{\mathrm{Miss}} = 0$ (see Fig. 7.2). The elastic asymmetries corresponding to the selected data-points were calculated using Eq. (2.27), and are presented in Fig. 7.13 (left). Determined ratios are shown in Fig. 7.13 (right). Results are nicely gathered around the predicted value (green line). They also agree with the data-points determined by the Mainz experiment [30]. By calculating the average value of the four data points (blue line), the effective proton polarization was estimated to be:

$$\langle P_p \rangle = -0.299 \pm 0.0173 \,,$$

which agrees well with a value predicted in Eq. (7.4). This speaks in favor of the devised toy model and indicates, that behavior of the $^3\vec{\mathrm{He}}(\vec{e}, e'p)d$ asymmetries at low missing momenta is understood.

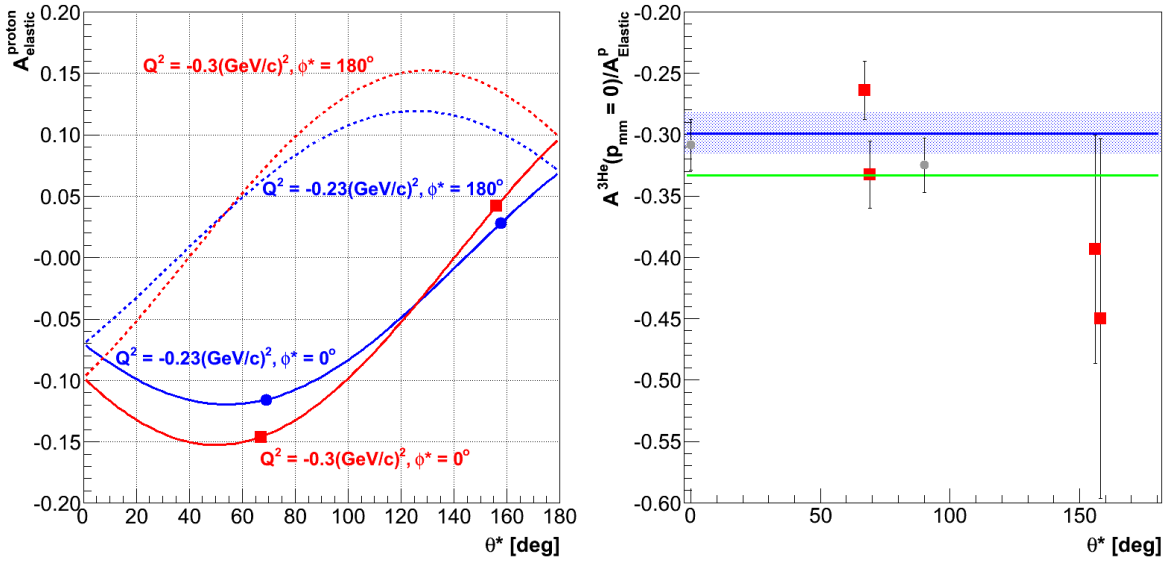

Figure 7.13 — [Left] The asymmetries $A^{\vec{e}\vec{p}}$ for elastic scattering of polarized electrons on polarized protons as functions θ^*, obtained from Eq. (2.27). Blue and red lines represent results for $Q^2 = -0.25\,(\mathrm{GeV/c})^2$ and $Q^2 = -0.35\,(\mathrm{GeV/c})^2$, respectively. Full and dotted lines distinguish between calculations performed for $\phi^* = 0°$ and $\phi^* = 180°$. Squares and circles show four points considered for the comparison with the measured helium asymmetries. [Right] Ratios (red squares) between the extracted 2BBU asymmetries at $p_{Miss} \approx 0$ and the corresponding elastic proton asymmetries. Green line represents the polarization of proton in a nucleus $P_p = -33.3\,\%$, predicted by the naive model. Blue line and surrounding band show the average of the four data points and its uncertainty. Gray circles represent data-points obtained by the Mainz experiment [30].

7.3 The three-body breakup channel $^3\vec{\mathrm{He}}(\vec{e}, e'p)pn$

The Bochum/Krakow group has provided calculations also for the three-body breakup channel $^3\vec{\mathrm{He}}(\vec{e}, e'p)pn$. The predicted longitudinal and transverse asymmetries, which were obtained with an identical procedure as described in Sec. 7.1, are presented in Figs. 7.25 and 7.26. To be able to compare these calculations to the measured asymmetries, a separation of the 3BBU data from the 2BBU data is essential. As indicated already in Sec. 7.1, this can not be done without an additional input from a Monte-Carlo simulation.

First such attempt was performed by using MCEEP (Monte Carlo for (e,e'p)). It was designed by P. E. Ulmer [118] to simulate coincidence (e,e'X) experiments by averaging theoretical models over the experimental acceptance. It offers several different cross-section parameterizations for $^3\vec{\mathrm{He}}(\vec{e}, e'p)$ reactions. Unfortunately the standard version contains only implementations for the HRS spectrometers. To use it for the E05-102 experiment, the acceptance of the HRS-R spectrometer was broadened to emulate BigBite. However, with such cheat only simulation of the physics quantities at the target was possible. The simulation of the BigBite detector variables is impossible without a proper description of the spectrometer and its particle trasport from the target to the detector package.

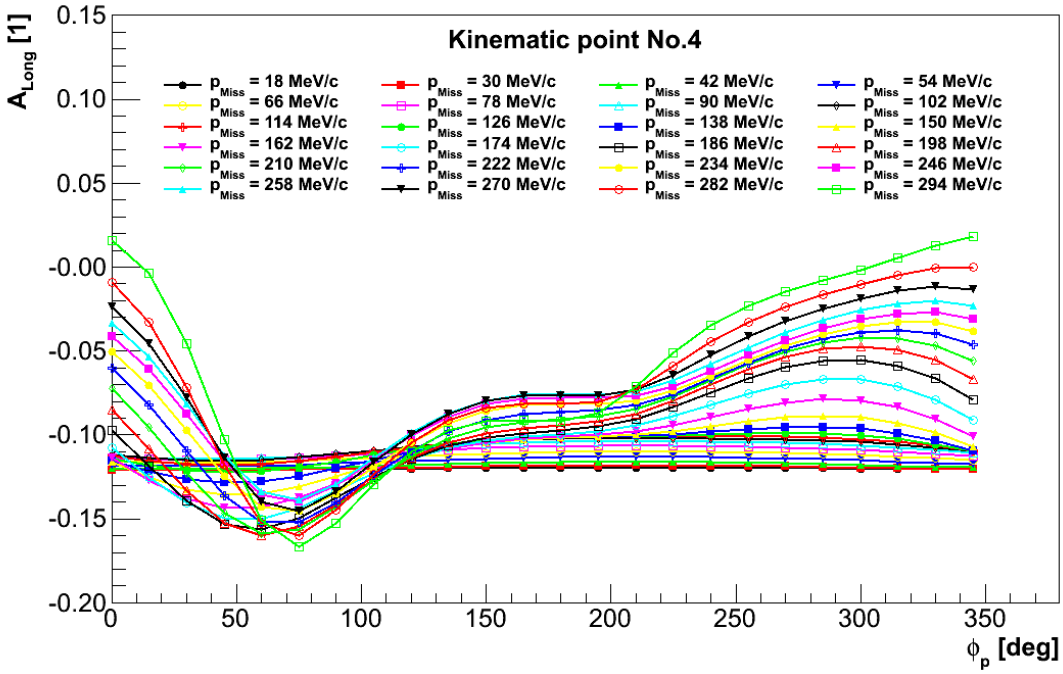

Figure 7.14 — The theoretical predictions for the longitudinal $^3\vec{\mathrm{He}}(\vec{e}, e'p)pn$ asymmetry $A_{Long} = A(\theta^* = 68°, \phi^* = 0°)$ as a function of an angle ϕ_p, for missing momenta up to $p_{Miss} \leq 300\,\mathrm{MeV}$. Presented are the asymmetries for the 4^{th} kinematic bin. Calculations were provided by the Bochum/Krakow group [117].

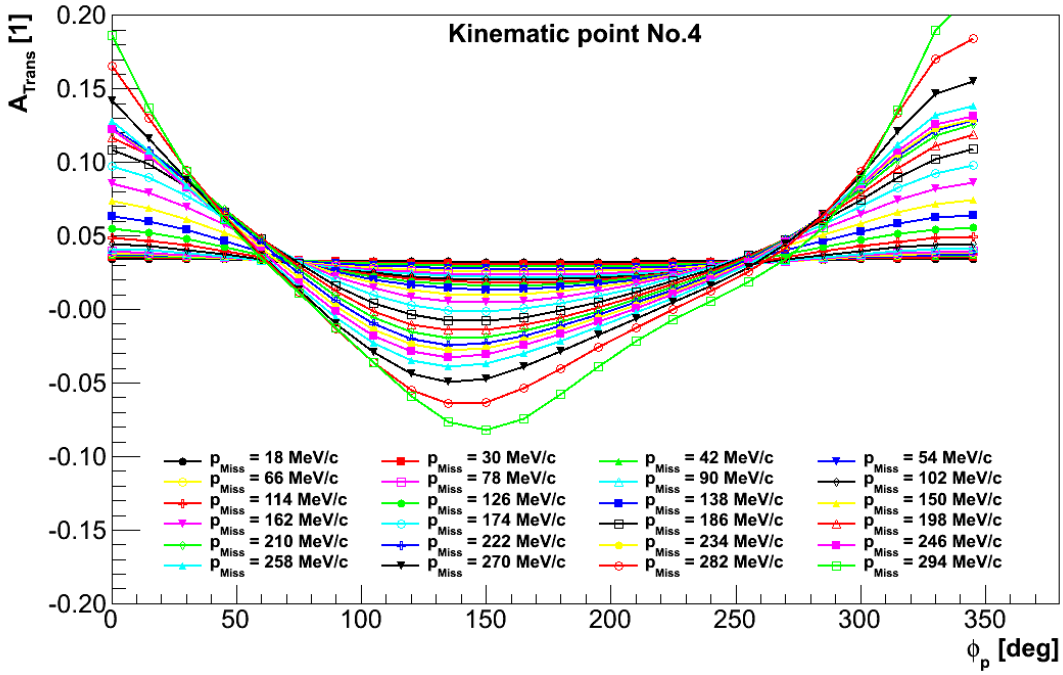

Figure 7.15 — The theoretical predictions for the transverse $^3\vec{\mathrm{He}}(\vec{e}, e'p)pn$ asymmetry $A_{Trans} = A(\theta^* = 156°, \phi^* = 0°)$ as a function of an angle ϕ_p, for missing momenta up to $p_{Miss} \leq 300\,\mathrm{MeV}$. Presented are the asymmetries for the 4^{th} kinematic bin. Calculations were provided by the Bochum/Krakow group [117].

Having these limitations in mind, MCEEP was run for our experimental conditions. Simulations for the two- and three-body breakup were run separately for the same amount of incident charge. The events from both simulations were then joined together to acquire a combined missing energy spectrum, that can be directly compared to the experimental data. Results of the simulation are shown in Fig. 7.16 (left). By comparing these to the experimental results shown in Fig. 7.1, one can see, that MCEEP significantly underestimates the width of the missing energy spectrum, even with the consideration of the radiative losses. The observed disagreement was attributed to the improper consideration of the spectrometer resolutions. To compensate for the difference in the widths, we decided to artificially broaden the generated peaks. This was accomplished by convoluting both missing energy peaks (2BBU and 3BBU) with the same Gaussian function. The width of the Gaussian distribution ($\sigma_{\text{Gauss}} = 4.3$) was chosen for the combined missing energy spectrum to agree best with the measured data. See Fig. 7.16 (right). The obtained results are now more reasonable. However, even with this correction, MCEEP is still unable to properly describe a strong, long tail present in the experimental data. This can be contributed to a known, but unsolved issue [119], that MCEEP underestimates the cross-section for the $^3\vec{\text{He}}(\vec{e}, e'\text{p})\text{pn}$ reaction. A correction to a cross-section for this process would raise the 3BBU peak in simulated missing energy spectrum, but would still require broadening of the peaks, due to the limited spectrometer resolutions.

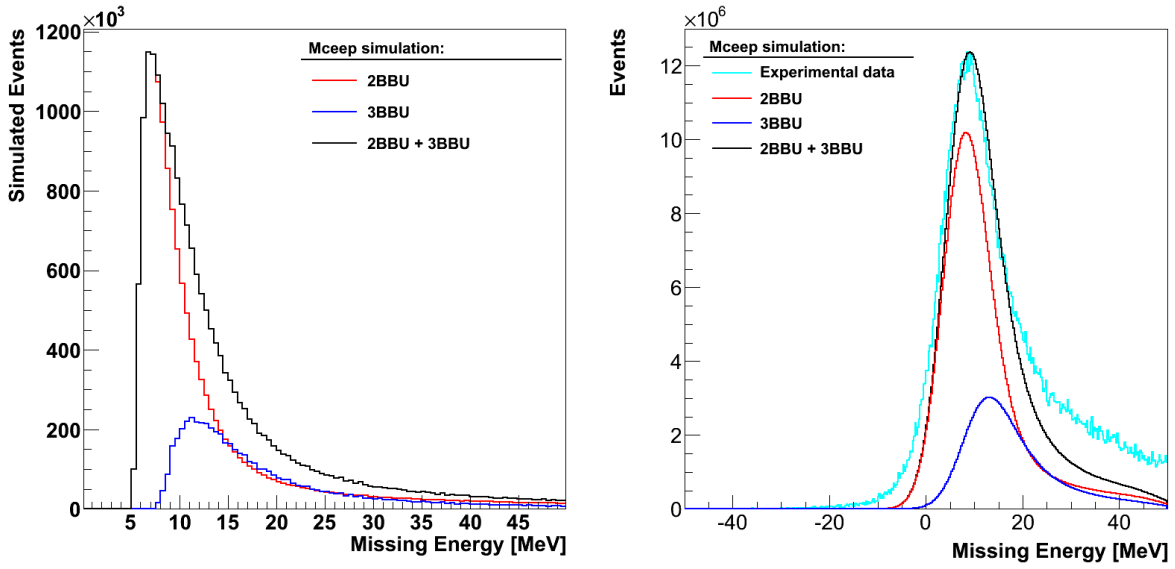

Figure 7.16 — [Left] The results of the MCEEP simulation for the $^3\vec{\text{He}}(\vec{e}, e'\text{p})\text{d}$ and $^3\vec{\text{He}}(\vec{e}, e'\text{p})\text{pn}$ reactions. The dominant part of the missing-energy peaks is contributed by the two-body reaction process. Even at very high missing energies, where the dominance of the 3BBU is expected, the 2BBU still contributes significantly to the cumulative distribution. The simulation also reveals, that even without any additional worsening of the resolution, the 3BBU contribution can not be distinguished from the main 2BBU peak. [Right] The results of the MCEEP simulation, after the convolution with a Gaussian function ($\sigma_{\text{Gauss}} = 4.3$) for obtaining more realistic resolutions. For the comparison, measured data are shown (cyan line). In spite of the applied corrections, the simulation is still unable to describe the observed strong tail on the right side of the peak.

The comparison of the broadened 2BBU and 3BBU missing energy peaks reveals,

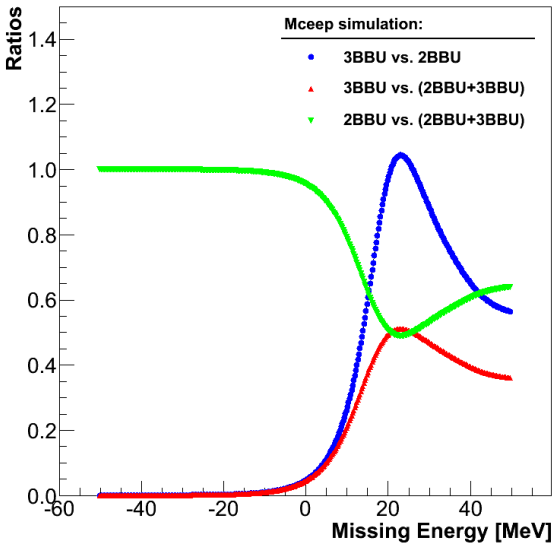

Figure 7.17 — The relative contributions of the 2BBU and 3BBU channel as a function of missing energies. The ratio between the number of two-body and three-body breakups is also shown. Results were obtained from the comparisons of the convoluted MCEEP results. In the region of negative missing energies, the two-body breakup dominates. The three-body breakups start contributing at positive missing energies, prevailing in the region of $20 \leq E_{Miss} \leq 40$. At very high E_{Miss}, where 3BBU losses its strength, the contribution of the 2BBU tail again becomes comparable to the 3BBU part.

that reduced resolution causes 3BBU events to appear also at missing energies below the theoretical threshold $E_{MeV} = 7.7\,MeV$. Fig. 7.17 shows the simulated ratio between the number of two-body and three-body breakups as a function of the missing energy. Although the contamination of 2BBU events with the 3BBU at $E_{Miss} \leq 2\,MeV$ seems to be small their contribution to the 2BBU asymmetry can not be neglected, because theory predicts large $^3\vec{He}(\vec{e}, e'p)pn$ asymmetries. Since the sign of the 3BBU asymmetries is opposite to the sign of the 2BBU asymmetries, such corrections could explain the unresolved discrepancy between the theory and measurements for the $^3\vec{He}(\vec{e}, e'p)d$ reaction.

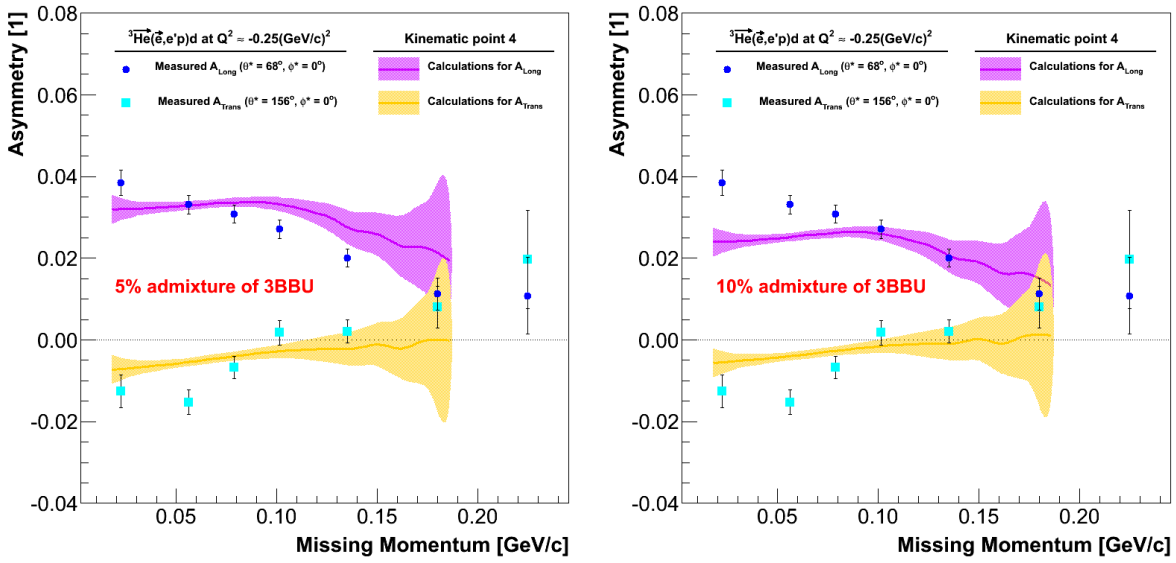

Figure 7.18 — Comparison of the theoretical 2BBU asymmetries, calculated for the 4th kinematic bin, to the extracted experimental asymmetries at $Q^2 = -0.25\,(GeV/c)^2$, when 5 % (left) and 10 % admixture of the $^3\vec{He}(\vec{e}, e'p)pn$ asymmetry is added to the calculations for the $^3\vec{He}(\vec{e}, e'p)d$ asymmetry. Labels as in Fig. 7.10

To test this assumption, the theoretical asymmetries for the $^3\vec{\mathrm{He}}(\vec{e},e'p)d$ reaction were added a 5 % and 10 % admixture of the $^3\vec{\mathrm{He}}(\vec{e},e'p)pn$ asymmetries. The modified asymmetries are presented in Fig. 7.18. As anticipated, a small contamination with the 3BBU asymmetries has caused a sizable change to the predicted 2BBU asymmetries. However, correction with a fixed ratio of the two-body and three-body breakups can be used only for demonstrative purposes. For a detailed analysis, an individual corrections to each bin in missing momentum are be required, since the ratio changes with the missing momentum (see Fig. 7.19). This again emphasizes an urgent need for a better and more trustworthy Monte-Carlo simulation, which could be used to adequately estimate the 3BBU/2BBU ratios, that are necessary for coupling theory to the data.

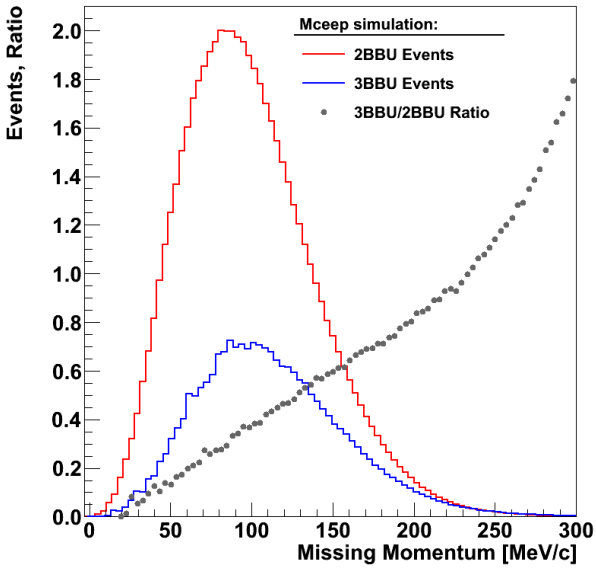

Figure 7.19 — Missing momentum distributions for the 2BBU and 3BBU-channels, obtained with the MCEEP simulation. Both distributions were scaled to 1/2 of the two-body breakup peak. No cuts on E_{Miss} were appriled and no corrections to the resolution werw considered. The ratio 3BBU/2BBU shows, that the contribution of the 3BBU grows with the missing momentum. Hence, the 3BBU correction to the 2BBU asymmetries will be largest at high missing momenta.

Although the results of the MCEEP simulation are not very convincing, we decided to use them in our pursuit of extracting information on the three-body breakup asymmetries, especially because this is the only simulation available at the moment. For this trial we have selected longitudinal and transverse data at $Q^2 = -0.35\,(\mathrm{GeV/c})^2$. Furthermore, we concentrated only on the events at low missing momenta ($p_{Miss} \leq 90\,\mathrm{MeV/c}$), that are shown in Fig. 7.2. High missing momentum data, were not yet analyzed. From the given data, we selected points with $E_{Miss} \geq 10\,\mathrm{MeV}$, because it is expected, that the 3BBU data will be most clearly accessible in that region. However, due to a large contamination with the 2BBU asymmetry, established in Fig. 7.17, the measured asymmetries A_{Exp} must be properly corrected for admixtures of 2BBUs. Assuming, that two-body breakup asymmetry A_{2BBU} is under control, the three-body asymmetry A_{3BBU} can be determined via [30]:

$$A_{3BBU}(E_{E_{Miss}}) = \frac{A_{Exp}(E_{Miss}) - A_{2BBU}\; p_{2BBU}(E_{Miss})}{1 - p_{2BBU}(E_{Miss})}, \tag{7.5}$$

where p_{2BBU} represents the relative amount of the 2BBU events in a particular E_{Miss} bin. The obtained results are gathered in Fig. 7.20. One can see, that applied corrections have a strong effect on the result and considerably increase the value of the asymmetry. This is consistent with the theoretical predictions of Bochum/Krakow group (see Fig. 7.25), which predict large negative asymmetries ($\sim -10\,\%$).

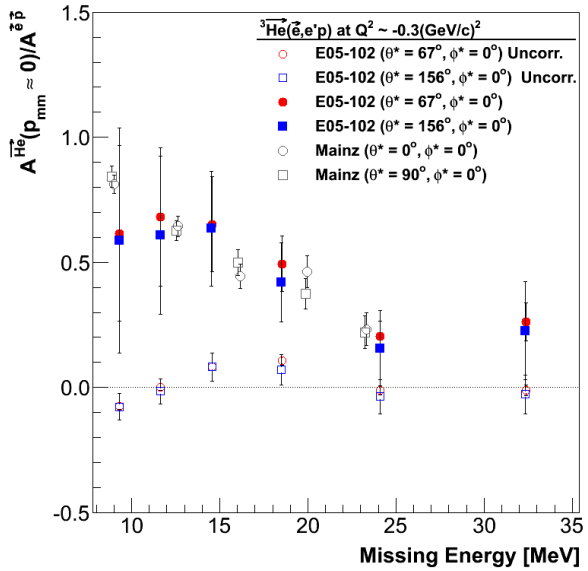

Figure 7.20 — Ratios of the $^3\vec{He}(\vec{e},e'p)pn$ asymmetries with the elastic proton asymmetries for the $Q^2 \approx -0.35\,(GeV/c)^2$ data. Hollow red and blue data-points show the 3BBU results before corrections for the 2BBU contamination. Full red and blue points show the corrected ratios. The results of the Mainz experiment [30] are demonstrated with gray hollow points. The significant worsening of the resolution for points at $E_{Miss} \approx 10\,MeV$ is predominantly caused by the small values of the denominator in Eq. (7.5) near the threshold for the 3BBU (see Fig. 7.17). The second most important contribution to the error is the estimated 20 % uncertainty of the two-body contamination factor p_{2BBU}, which is determined from MCEEP simulation.

Fig. 7.20 shows ratios of extracted 3BBU asymmetries, with the corresponding elastic proton asymmetries (see Fig. 7.13). The choosing of such interpretations gives us ability to compare the obtained results with those from the Mainz experiment [30]. Their measurements were performed at very similar kinematic conditions ($Q^2 \approx -0.3\,(GeV/c)^2$, $\omega = 135\,MeV$, $|\vec{q}| = 570\,MeV/c$, $p_{Miss} \approx 40\,MeV/c$). However, their data were collected for different target spin orientations ($\theta^* = 0°\,,\ 90°$), resulting in much larger absolute values of the asymmetries (see Fig. 7.21). To make both results comparable, the normalization with the elastic proton asymmetry was chosen. In Fig. 7.20, the Mainz ratios are presented with the gray hollow circles and squares, and show good agreement with our results.

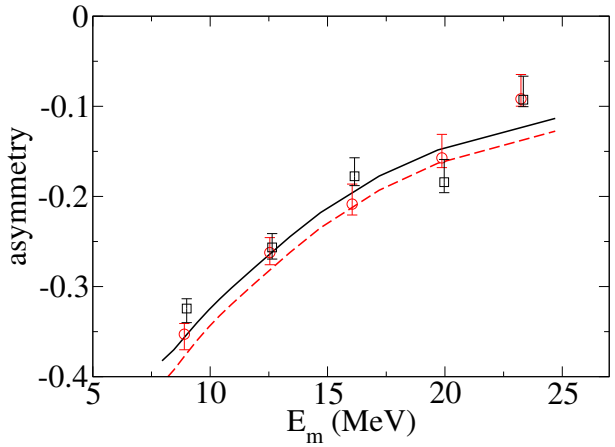

Figure 7.21 — The Mainz results for the parallel and perpendicular asymmetry as a function of missing energy E_m in the 3BBU-channel. $A(\theta^* = 0°, \phi^* = 0°)$: data (squares), theory (solid line). $A(\theta^* = 90°, \phi^* = 0°)$: data (circles), theory (dasled line). [30]

Before precise theoretical calculations were available, this illustration, together with results shown in Fig. 7.13, served for convincing our selves, that the asymmetries obtained with the E05-102 experiment are not unreasonable. Now, that theoretical predictions are accessible, more detailed comparison with the data is possible, also for the missing momenta $p_{Miss} \geq 0$. As demonstrated with this first attempt, the extraction of the 3BBU asymmetries requires both accurate simulation and good understanding

of the experimental data. Hence, it represents another important challenge for the upcoming analysis.

7.4 The deuteron channel $^3\vec{\mathrm{H}}\mathrm{e}(\vec{e}, e'\mathrm{d})\mathrm{p}$

The comparison of the measured $^3\vec{\mathrm{H}}\mathrm{e}(\vec{e}, e'\mathrm{d})\mathrm{p}$ asymmetries with the theoretical calculations of Bochum/Krakow group was carried out with an approach, identical to the one used for the interpretation of the proton channels. The asymmetries for each calculated kinematic point were again individually examined. Since the majority of the events for this reaction channels is gathered inside the top three kinematic bins (see Fig. 7.22), we limited our present analysis to kinematic points 5, 8 and 11.

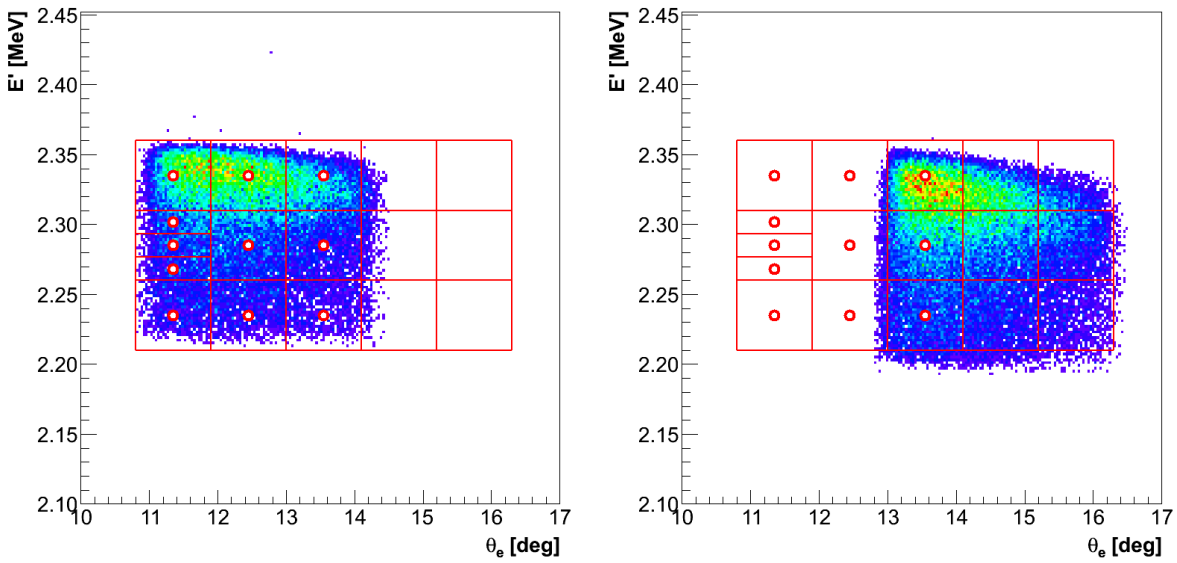

Figure 7.22 — The available electron kinematics for the $^3\vec{\mathrm{H}}\mathrm{e}(\vec{e}, e'\mathrm{d})\mathrm{p}$ reaction. Left and right plots show results when HRS-L was positioned at $\theta_{\mathrm{HRS-L}} = 12.5°$ and 14.5°, respectively. The whole kinematical coverage was divided into 17 bins, shown with red squares. Theoretical calculations were performed for the centers of first 11 bins (demonstrated with circles).

Similarly as for the proton channel, correct pairs of deuteron kinetic energies T_d and polar angle θ_d had to be submitted to the code, in order for the theoretical calculations to be executed for a desirable set of missing momenta. Selected points for the 5^{th} kinematic bin are shown in Figs. 7.23 and 7.24. Again, not all missing momenta are accessible with each kinematic point. Some may be prohibited by the equations (7.1) and (7.2). Histograms belonging to $p_{\mathrm{Miss}} < 78\,\mathrm{MeV/c}$ therefore do not contain theoretical points. On the other hand are the experimental data not limited to a single kinematic point. They are smeared over the selected kinematic bin (red squares in Fig. 7.22). This gives them enough freedom to appear also in histograms with smaller missing momenta.

In the sense of missing momenta is the 11^{th} kinematic point the most interesting one, because it is the only theoretical point, where asymmetries at very low missing momenta are accessible. The calculated longitudinal and transverse asymmetries for

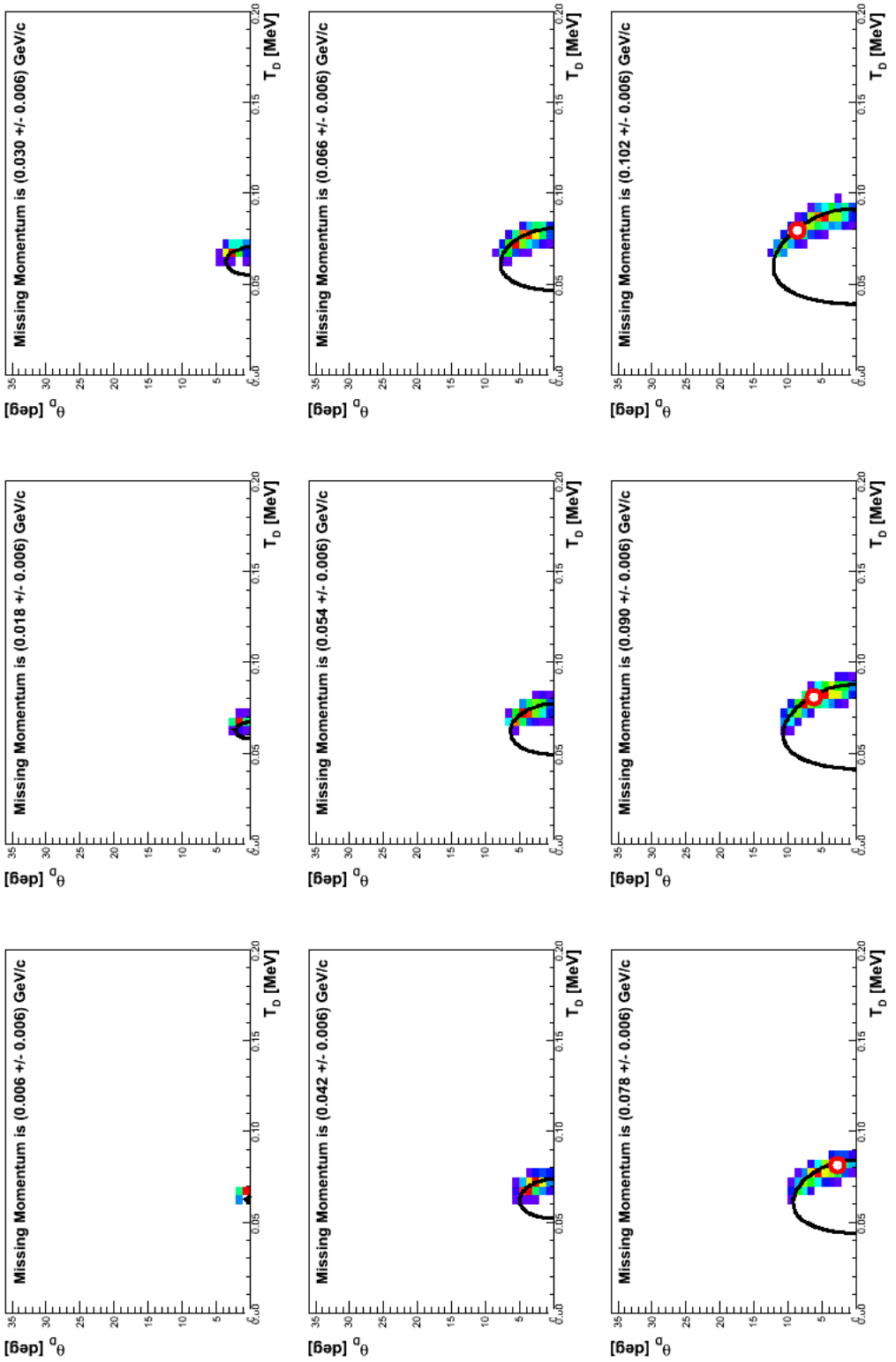

Figure 7.23 — Two-dimensional histograms showing the relation between deuteron angle θ_d and its kinetic energy $T_d \approx p_d^2/2M_d$ for selected bins in p_{Miss}. In these plots data surrounding the 5^{th} kinematics point were considered (see Fig. 7.4). The lengths of obtained bands are controlled by the remaining spread in ω and $\vec{q}$. Black lines show solutions of Eq.(7.2) for a given p_{Miss} and $|\vec{q}| = 485.0\,\mathrm{MeV/c}$. Circles show $(\theta_d, \tilde{p}_d)$ pairs considered in the theoretical calculations. In a selected kinematic point, theoretical points at very low missing momenta are not permitted. Therefore, theoretical points are missing in first six histograms.

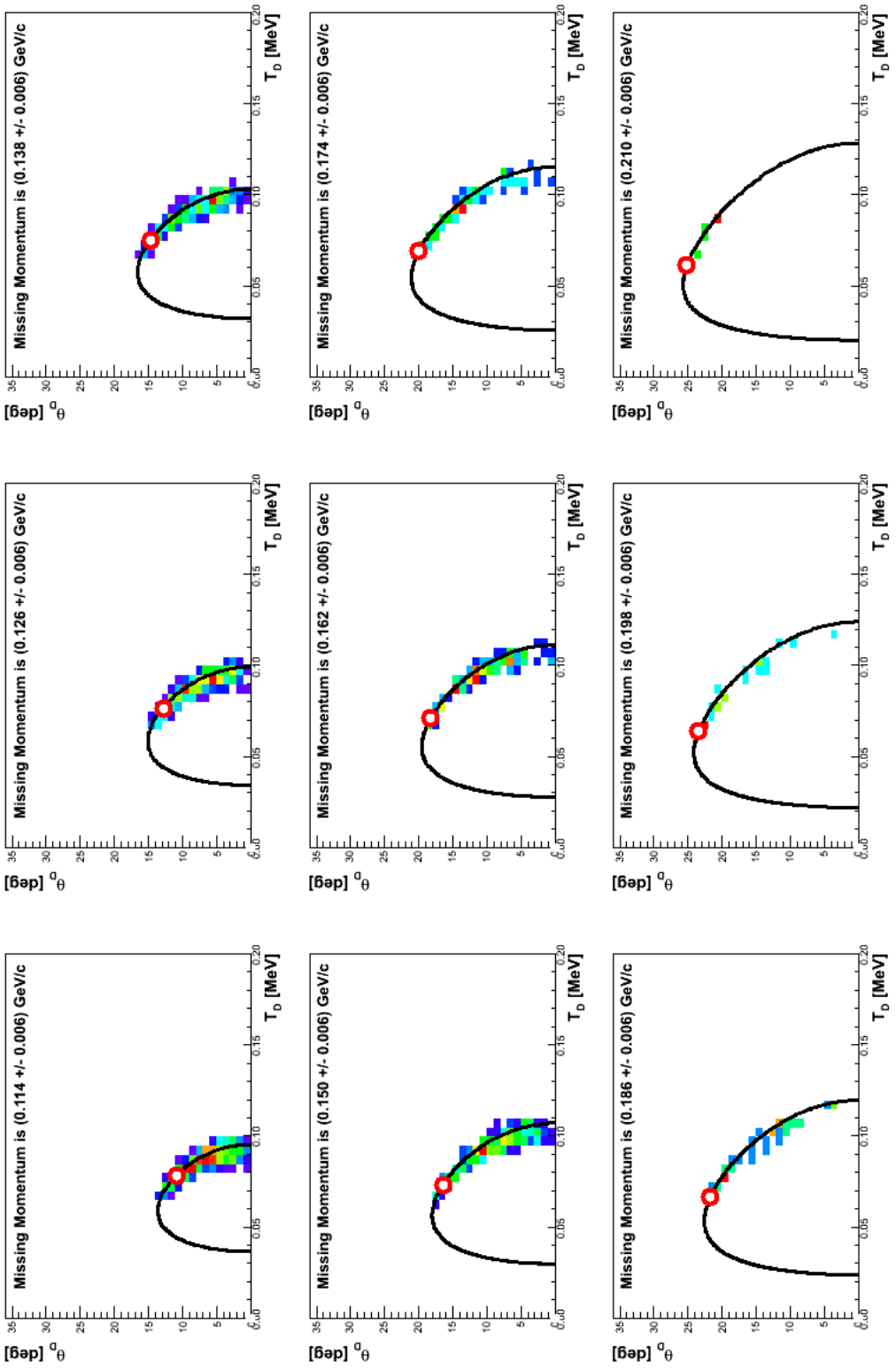

Figure 7.24 — Two-dimensional histograms showing the relation between deuteron angle θ_d and its kinetic energy $T_d \approx p_d^2/2M_d$ for selected bins in p_{Miss}. In these plots data surrounding the 5^{th} kinematics point were considered (see Fig. 7.4). The lengths of obtained bands are controlled by the remaining spread in ω and $\vec{q}$. Black lines show solutions of Eq.(7.2) for a given p_{Miss} and $|\vec{q}| = 485.0\,\mathrm{MeV/c}$. Circles show $(\theta_d, \tilde{p}_d)$ pairs considered in the theoretical calculations.

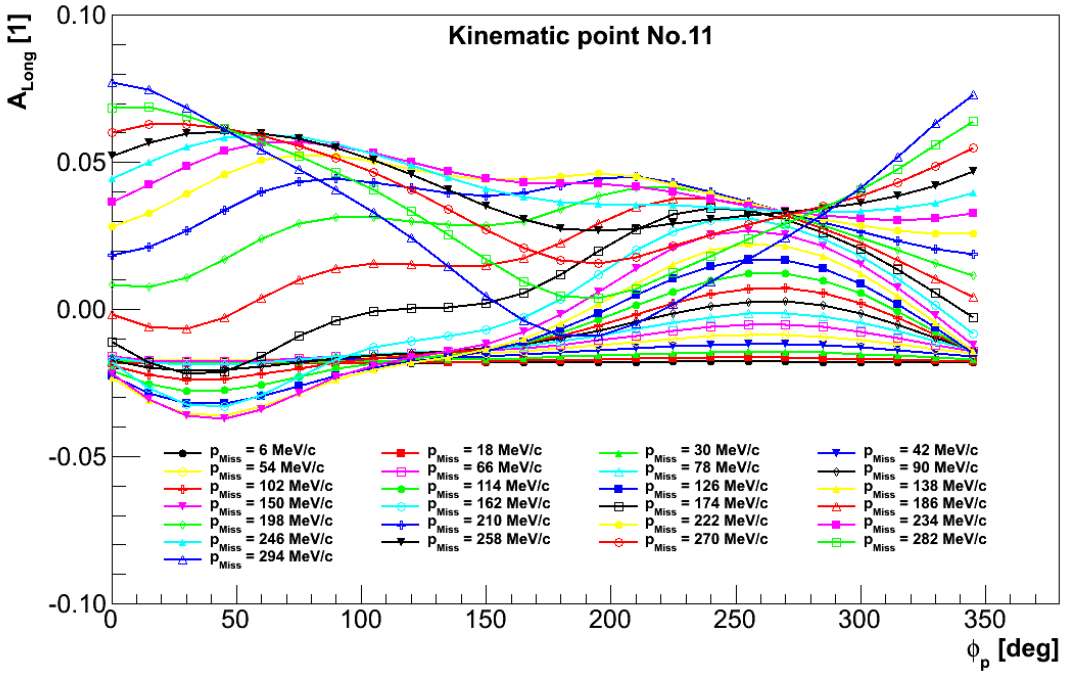

Figure 7.25 — The theoretical predictions for the longitudinal $^3\vec{\mathrm{He}}(\vec{e}, e'\mathrm{d})\mathrm{p}$ asymmetry $A_{\mathrm{Long}} = A(\theta^* = 73°, \phi^* = 0°)$ as a function of an angle ϕ_p, for missing momenta up to $p_{\mathrm{Miss}} \leq 300\,\mathrm{MeV}$. Presented asymmetries were obtained for the 11^{th} kinematic bin. Calculations were provided by the Bochum/Krakow group [117].

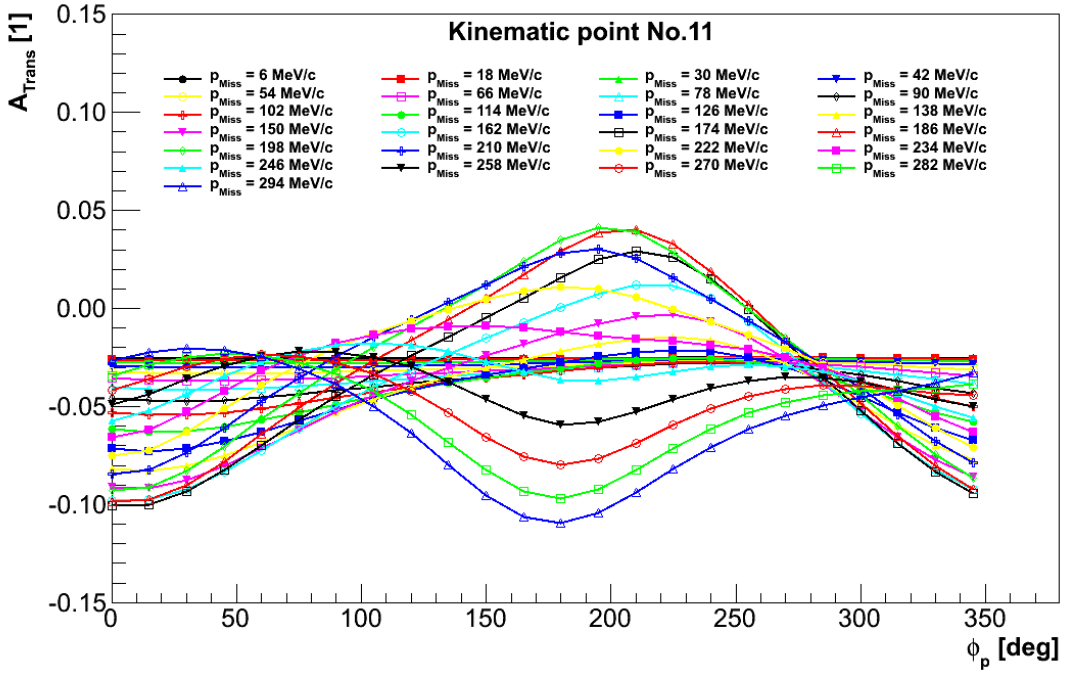

Figure 7.26 — The theoretical predictions for the transverse $^3\vec{\mathrm{He}}(\vec{e}, e'\mathrm{d})\mathrm{p}$ asymmetry $A_{\mathrm{Trans}} = A(\theta^* = 163°, \phi^* = 0°)$ as a function of an angle ϕ_p, for missing momenta up to $p_{\mathrm{Miss}} \leq 300\,\mathrm{MeV}$. Presented asymmetries were obtained for the 11^{th} kinematic bin. Calculations were provided by the Bochum/Krakow group [117].

this kinematic point are gathered in Figs. 7.23 and 7.24. In order to compare these computations to the experimenatal asymmetries, averaging over the ϕ_d angle needs to be performed for each p_{Miss}, analogously as it was done for the proton channel. Here the ϕ_d represents an angle between the scattering plane and the reaction plane, which is this time determined by the deuteron momentum and vector $\vec{q}$ (see Fig. 2.2). Examples of the ϕ_d distributions for various missing momenta are presented in Fig. 7.27.

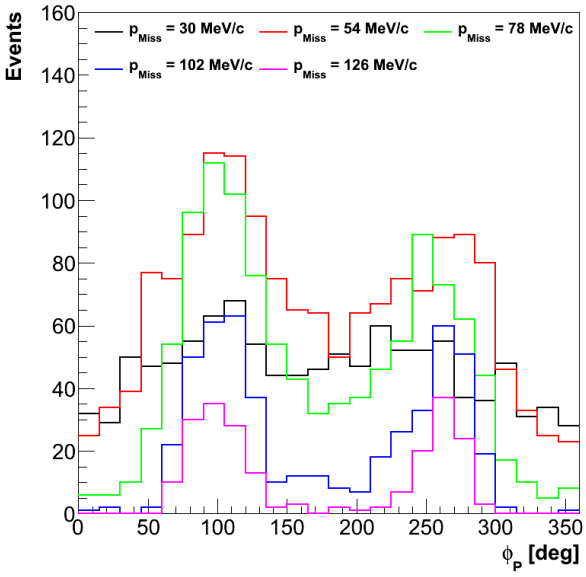

Figure 7.27 — The distributions of ϕ_d at different p_{Miss}, determined for the events gathered around the 11th kinematic point. At low missing momenta are events uniformly distributed over whole angular range. At high missing momenta, events with $\phi_d \approx 90°, 270°$ dominate.

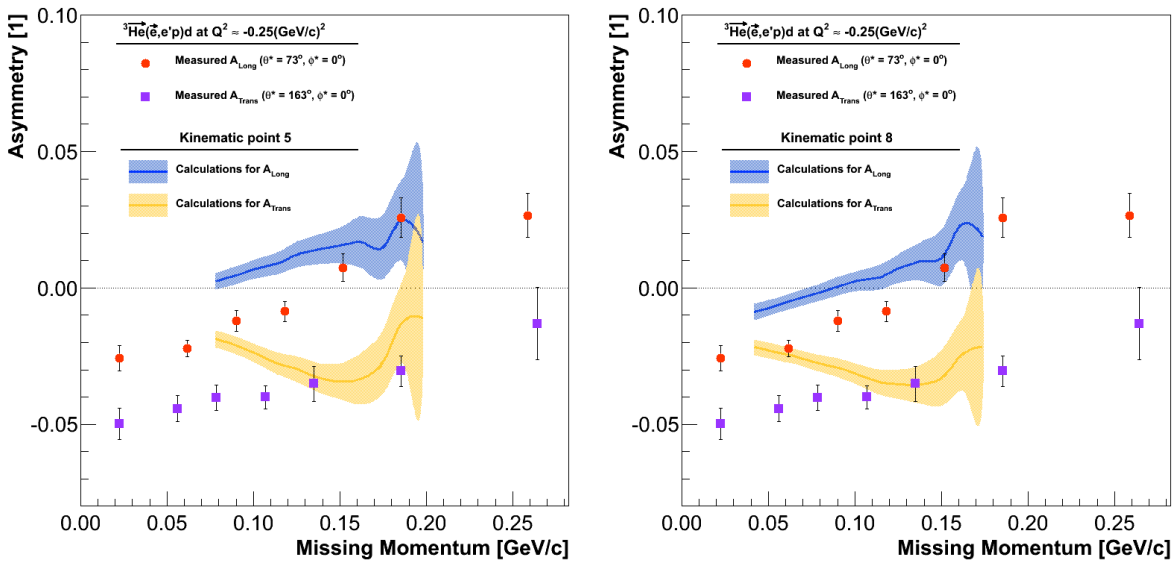

Figure 7.28 — Comparison of the theoretical $^3\vec{He}(\vec{e}, e'd)p$ asymmetries, calculated for 5th (left) and 8th kinematic bin, with the experimental asymmetries at $Q^2 = -0.25\,(GeV/c)^2$. The theoretical asymmetries are shown with full lines. The surrounding bands demonstrate the uncertainties of the predicted asymmetries. Errors are governed by statistics of the ϕ_d-histograms (see Fig. 7.27) used for the averaging of the calculated asymmetries over the angle ϕ_d.

Once the theoretical calculations were properly weighted with and averaged over ϕ_d, they could be compared to the measured data. Results for the three considered

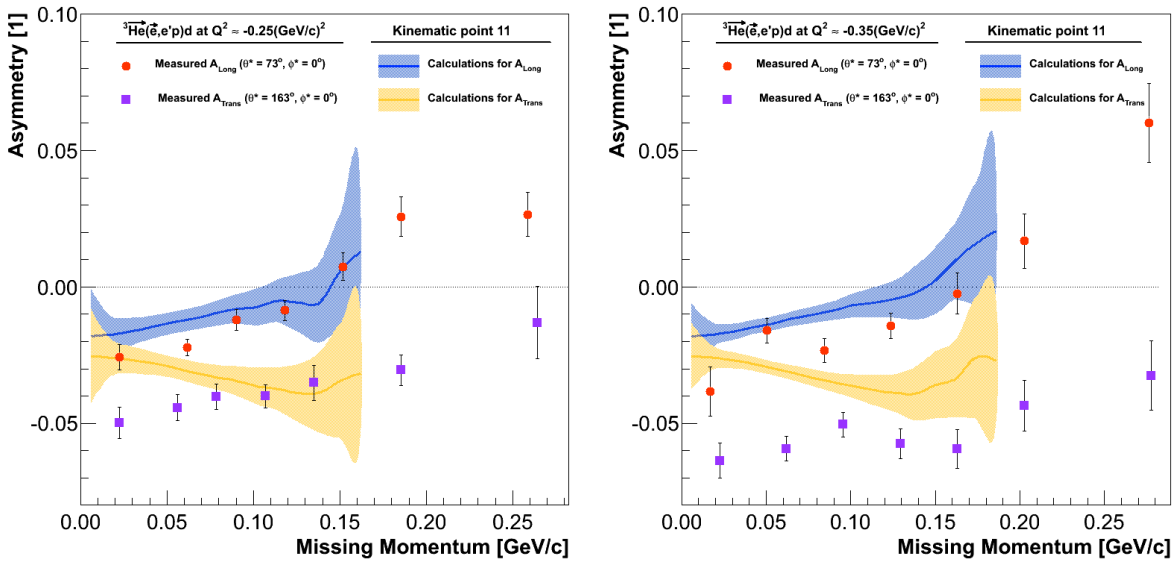

Figure 7.29 — Comparison of the theoretical $^3\vec{He}(\vec{e},e'd)p$ asymmetries, calculated for the 11^{th} kinematic bin, with the experimental asymmetries at $Q^2 = -0.25\,(GeV/c)^2$ (left) and $Q^2 = -0.35\,(GeV/c)^2$ (right). The theoretical asymmetries are shown with full lines. The surrounding bands demonstrate the uncertainties of the predicted asymmetries. Errors are governed by statistics of the ϕ_d-histograms (see Fig. 7.27) used for the averaging of the calculated asymmetries over the angle ϕ_d.

theoretical bins are shown in Figs. 7.28 and 7.29. Both $Q^2 = -0.25\,(GeV/c)^2$ and $Q^2 = -0.35\,(GeV/c)^2$ data were put to the test. The theory does not agree with the data. The measured and predicted asymmetries have consistent signs. They also agree in the position of the zero-crossing point. Otherwise they do not match. Even at very low missing momenta, where the best agreement was expected, the theory predicts much smaller transverse asymmetry ($\approx 2.5\,\%$) as it was measured ($\approx 5\,\%$). Opposite are also trends of both asymmetries. Furthermore, inconsistent with the measurements are also predictions for the longitudinal asymmetry. The disagreement worsens when moving to smaller Q^2.

Unfortunately for the deuteron channel, the interpretation of the measured results is limited to the comparison with the full theoretical calculations. Primitive models, analogous to the one considered for the proton channel (see Sec. 7.2), can not be applied, because it was shown by previous experiments (see Fig. 1.6) and the theory (see Sec. 2.5), that deuteron pole diagram does not provide satisfactory description of the $^3\vec{He}(\vec{e},e'd)p$ process at low missing momenta. Hence, we need to relay on the sophisticated theoretical models, and try to reason the results.

Inconsistencies between the theory and the measurements in this first iteration of the analysis are not unexpected. The measurements presented in this thesis are first of its kind, which means, that so far theoreticians had no proper reference point for the calibration of their theories. However, in the following analysis these discrepancies will have to be addressed. This will require further analysis and tests of the measured data, as well as the improvements in the theoretical calculations. Hopefully in the end the theory and the measurements will converge. At this point, independent calculations from other theoretical groups would also be very beneficial for finding the root of

the discovered disagreements. We already received calculations from Hannover group, but have not been able yet to correctly interpret their results. Therefore they are not presented in this thesis.